Plasmonic Au@Pd nanorods with boosted refractive index susceptibility and SERS efficiency : a multifunctional platform for hydrogen sensing and monitoring of catalytic reactions

Plasmonic Au@Pd nanorods with boosted refractive index susceptibility and SERS efficiency: A multifunctional platform for hydrogen sensing and monitoring of catalytic reactions

Sergio Rodal-Cedeira,[1] Verónica Montes-García,[1] Lakshminarayana Polavarapu,[2,3] Diego Martínez Solís,[4] Hamed Heidari,[5] Andrea La Porta,[5] Marco Angiola,[6] Alessandro Martucci,[6] José M. Taboada,[7] Fernando Obelleiro,[4] Sara Bals,[5] Jorge Pérez-Juste,[1,*] Isabel Pastoriza-Santos[1,*]

[1] Departamento de Química Física and CINBIO, Universidade de Vigo, 36301 Vigo, Spain

[2] Chair for Photonics and Optoelectronics, Department of Physics and Center for Nanoscience (CeNS), Ludwig-Maximilians-Universität (LMU), Amalienstraße 54, 80799 Munich, Germany

[3] Nanosystems Initiative Munich (NIM), Schellingstraße 4, 80799 Munich, Germany

[4] Departamento de Teoría de la Señal y Comunicaciones, Universidade de Vigo, 36310 Vigo, Spain

[5] EMAT, University of Antwerp, Groenenborgerlaan 171, B-2020 Antwerp, Belgium

[6] Università di Padova - Dipartimento di Ingegneria Industriale, via Marzolo 9, 35131 Padova, Italy

[7] Departamento Tecnología de los Computadores y de las Comunicaciones, Universidad de Extremadura, 10003 Cáceres, Spain

Abstract

Palladium nanoparticles (Pd NPs) have received tremendous attention over the years due to their high catalytic activity for various chemical reactions. However, unlike other noble metal nanoparticles such as Au and Ag NPs, they exhibit poor plasmonic properties with broad extinction spectra and less scattering efficiency, and thus limiting their applications in the field of plasmonics. Therefore, it has been challenging to integrate tunable and strong plasmonic properties into catalytic Pd nanoparticles. Here we show that plasmonic Au@Pd nanorods (NRs) with relatively narrow and remarkably tunable optical responses in NIR region can be obtained by directional growth of Pd on penta-twinned Au NR seeds. We found that the presence of bromide ions facilitates the stabilization of facets for the directional growth of Pd shell to obtain Au@Pd nanorods (NR) with controlled length scales. Interestingly it turns out that the Au NR supported Pd NRs exhibit much narrow extinction compared to pure Pd NRs, which makes them suitable for plasmonic sensing applications. Moreover, these nanostructures display, to the best of our knowledge, one of the highest ensemble refractive index sensitivity reported to date (1067 nm per refractive index unit, RIU). Additionally, we showed the application of such plasmonic Au@Pd NRs for localized surface plasmon resonance (LSPR)-based sensing of hydrogen both in solution as well as on substrate. Finally, we demonstrate that the integration of excellent plasmonic properties in catalytic palladium enables the *in situ* monitoring of a reaction progress by surface-enhanced Raman scattering. We believe that the proposed approach to boost the plasmonic properties of Pd nanoparticles (NPs) will ignite the design of complex shaped plasmonic Pd NPs to be used in various plasmonic applications such as sensing and *in situ* monitoring of various chemical reactions.

INTRODUCTION

Noble metal nanoparticles (NPs) have received enormous attention during the last two decades due to their unique optical properties that arise from the localized surface plasmon resonance (LSPR).[1-3] Their plasmonic properties have been widely explored for wide range of applications. However, most of the studies on plasmonics have been focused mainly on Au and Ag. Other noble metals such as Pd and Pt have been seldom explored due to their poor plasmonic properties in the visible-NIR region compared to Au and Ag.[4] On the other side, palladium has become a technologically important metal because of its extensive use in numerous industrial applications of catalysis.[5,6] Additionally, Pd-based materials have also been highly used in hydrogen purification, storage and detection, and fuel cells due its ability to reversibly absorb large quantities of hydrogen through hydride formation at ambient condition.[7,8] Driven by these interesting applications, there has been a growing interest in making plasmonically efficient multifunctional Pd-based nanoparticles for *in situ* hydrogen sensing and optical probing of chemical reactions. Such processes can be monitored through LSPR shifts of the plasmonic Pd NPs caused by permittivity changes of the metal or by surface-enhanced Raman scattering (SERS) signals of the molecules, respectively.[9-12] In fact palladium NPs exhibit plasmonic properties that are tunable from ultraviolet to infrared wavelengths. However their efficiency is rather low due to large plasmonic losses, and broad and asymmetric extinction spectra. For this reason, most of the reported plasmonic SERS or LSPR sensors are based on either Au or Ag NPs.[1,3,13] In the case of LSPR based sensors their sensing capabilities are mainly determined by the refractive index sensitivity, defined as the shift of the LSPR per refractive index unit (RIU), and the figure of merit (FOM), defined by the ratio between the refractive index sensitivity and the full width at half maximum of the LSPR band. Both parameters are largely dependent on the aspect ratio of the nanoparticles, which determines the location of the LSPR, more than on the shape, size.[14,15] So, there has always been a quest for morphologies and new metals with enhanced refractive index susceptibility. Taking into account that Pd exhibit higher refractive index sensitivity than Au and Ag due to the small dispersion of the real part of the Pd dielectric function,[16] anisotropic Pd nanoparticles with NIR extinction would be ideal for

plasmon-enhanced sensing applications.[16,17] However, their poor plasmonic properties limit their potential applicability. Therefore, obtaining plasmonically active Pd nanoparticles with relatively narrow extinctions has been extremely challenging and it is a dream for researchers.

In this regard, there has been a growing interest in bimetallic NPs for the incorporation of two or more properties in one nanostructure. Recently, RI sensitivity of bimetallic nanoparticles of Au/Pd with various morphologies such as stars and core-shell NPs has been investigated.[10-12,16,18-21] However, there is a significant room for improving the refractive index sensitivity and FOM with particles that shows narrow extinction in NIR region.[14,22]

In this work, we show that the NIR plasmonic properties of Pd nanorods (NRs) can be greatly enhanced by incorporating Au NR into them, without affecting the LSPR frequency of pure Pd NRs. For this reason we developed a strategy to fabricate Au@Pd NRs with tunable optical properties in the NIR region using penta-twinned (PTW) Au NRs as seeds and Br^- as directional growth agent. We found that the Au@Pd NRs exhibit significantly enhanced RI susceptibility compared to Au NRs of similar LSPR wavelength. These Au@Pd NRs exhibit one of the highest refractive index sensitivity (1065 nm/RIU) ever reported for a nanoparticle system till date.[12,14] More importantly, the narrow extinction of Au@Pd NRs leads to a great enhancement in the FOM compared to pure Pd NRs. The results reported are well supported by theoretical calculations performed using core-shell Au@Pd NRs as model. Furthermore, the application of Au@Pd NRs, in colloidal suspension or deposited on a glass substrate, for optical sensing of hydrogen has been demonstrated. Additionally, while acting as catalysts itself, the Au@Pd heterostructures enabled the optical monitoring of 4-NTP catalytic hydrogenation by *in situ* SERS spectroscopy, revealing the ability to act as efficient multifunctional platform with enhanced catalytic activity.

EXPERIMENTAL SECTION

Materials: Hexadecyltrimethylammonium bromide (CTAB, ≥96.0 %), Hydrogen tetrachloroaurate trihydrate ($HAuCl_4$ 3 H_2O), hexadecyltrimethylammonium chloride (CTAC, 25 % in water), silver nitrate ($AgNO_3$, ≥ 99.0 %), L-ascorbic acid (AA, ≥ 99 %), sodium borohydride ($NaBH_4$, 99 %), sodium citrate dihydrate (≥ 98 %), palladium (II)

chloride (99%), hydrogen peroxide solution (35 wt % in H_2O), poly(diallyldimethylammonium chloride) solution (PDDA, Mw 100,000-200,000, 20wt%), poly(styrenesulfonate) (PSS, Mw 70,000), sodium chloride (NaCl), glycerol(≥ 99 %) were purchased from Aldrich. Hydrocloric acid (HCl, 37%) and sulfuric acid (H_2SO_4, 95-97%) were supplied by Scharlau. Poly(vinylpyrrolidone) (PVP K30 Mw 40,000) was procured by Fluka. All chemicals were used as received. Pure grade ethanol and Milli-Q water with a resistivity of >18.2 MΩ cm were used throughout the experiments.

Methods: ***Synthesis of PTW Au NRs.*** Pentatwinned Au NRs were prepared following a previously published protocol with minor modifications.[23] Briefly, in a first step a 3.5 nm Au citrate seed solution was prepared as follows: 20 mL of growth solution containing 1.25 x 10^{-4} M $HAuCl_4$ and 2.50 x 10^{-4} M trisodium citrate was prepared in a conical flask at room temperature. Next, 0.3 mL of 0.01 M $NaBH_4$ solution was added to the solution while vigorous stirring. The stirring was slowed down after 30 s and for the next 15 min the Au sol was stirred gently at 40-45 ^oC to ensure removal of $NaBH_4$ excess. In a second step, a 5.5 nm Au CTAB nanoparticle solution was prepared as follows: 5 mL of growth solution consisting of 1.25 x 10^{-4} M $HAuCl_4$ and 0.040 M CTAB at 25-30 ^oC was mixed under stirring with 0.0125 mL of 0.10 M ascorbic acid. 1.67 mL of 3.5 nm Au citrate seed was then added quickly to the solution while stirring. In the final step, PTW gold nanorods were grown as follows; 1L growth solution ([$HAuCl_4$] = 1.25 x 10^{-4} M and [CTAB] = 0.008M) was thermostated at 20 ^oC. Next, 2.5 mL of 0.1 M ascorbic acid was added to the growth solution and mixed thoroughly. After homogenization, 4 mL of seed 5.5 nm Au-CTAB seed solution was added and allowed to react for several hours.

After the synthesis, PTW Au NRs were centrifuged (10 min 6,500 rpm), the supernatant was discarded and the precipitate redispersed in 10 mL. PTW Au NR were purified by adding a volume of 25 wt% CTAC to obtain 0.12 M (final concentration) leading to the flocculation of PTW Au NRs by depletion forces. Afterwards, the supernatant was then removed and the precipitate was re dispersed in 15 mL Milli-Q water.

Synthesis of Au@Pd NRs**:** Initially, a 5 mM solution of H_2PdCl_4 was prepared by dissolving $PdCl_2$ in 10 mM HCl solution. The Au@Pd NRs were prepared used a seeded

growth method. In a standard synthesis, 60 µL of HCl 100 mM, 42 µL of 5 mM H_2PdCl_4 and 150 µL of ascorbic acid 40 mM were added to 3 mL of seed solution containing 0.050 mM PTW Au NRs (in terms of gold) and 10.8 mM CTAB. Afterwards, the reaction mixture was heated at the desired temperature (see Figure S5 in SI). The amount of Pd salt added was varied from 21, 42 to 84 µL of 5 mM H_2PdCl_4 while the other conditions were kept the same for all synthesis. After the synthesis, the Au@Pd NRs were centrifuged (10 min 6,500 rpm) and redispersed in water.

***Deposition of Au@Pd NR on glass substrates*:** Prior to the deposition on the glass substrates Au@Pd NRs were coated with PVP by first centrifuging (8,000 rpm, 20 min) and redispersing in Milli-Q water, followed by dropwise addition of a PVP aqueous solution, previously sonicated during 15 min ([Au]/[PVP] ratio 1.5), under vigorous stirring. The mixture was gently stirred overnight and then centrifuged (1,500 rpm, 2h) and redispersed in ethanol under sonication.

Microscope glass slides were used as substrates, so as to allow UV-vis-NIR spectroscopy measurements. The substrates were sonicated for 10 min in water and then in ethanol, subsequently thoroughly cleaned using piranha solution (H_2SO_4: H_2O_2=7:3), rinsed with deionized water, and dried under an air stream. The slides were stored in water until use. For the assembly of nanorods, the slides were first immersed in an aqueous solution of positively charged PDDA (1 mg/mL in 0.5 M NaCl aqueous solution) for 20 min, then in an aqueous solution of the negatively charged PSS (Mw 70 000, 1 mg/mL in 0.5 M NaCl aqueous solution) for 10 min, and finally in PDDA solution for 10 min. At this stage, the slides are positively charged, favoring the electrostatic interactions with negatively charged nanorods. To obtain a monolayer of gold nanorods, the pretreated slides were immersed into the corresponding colloid for a suitable period time. After each adsorption step, the substrates were rinsed with water and dried under an air stream.

Plasma treatment with O_2: To remove the CTAB and PVP molecules on the surface of the Au nanorods, the deposited arrays were treated in the plasma cleaner for 5 min at 18 W. The plasma-cleaning conditions were adapted to ensure that the organic molecules are completely removed while the shape of the Au nanorods and Au@Pd nanorods remain unchanged as revealed by SEM characterization (Figure S10).

Characterization Techniques: Optical characterization was carried out by UV-vis-NIR spectroscopy with either Agilent 8453 or Cary 5000 spectrophotometers. TEM images were obtained with a JEOL JEM 1010 transmission electron microscope operating at an acceleration voltage of 100 kV. SEM images were obtained using a JEOL JSM-6700F FEG scanning electron microscope operating at an acceleration voltage of 5.0 kV for secondary-electron imaging (SEI). Tilt series for 3D tomography were acquired using either a FEI Tecnai G2 and FEI Osiris microscopes, operated at 200 kV. A single tilt tomography holder (Fischione model 2020) was used for acquisition, and the alignment and reconstruction were carried out using the FEI Inspect3D software and the ASTRA toolbox. HAADF-STEM images were acquired using a double aberration corrected Titan 50−80 microscope operating at 300 kV in STEM mode.

Numerical simulations: Extinction spectra simulations for Au NR and Au@Pd NR were obtained using a full-wave frequency-domain approach based on boundary-element parameterizations (SIE-MOM),[24,25] which greatly reduce the resulting algebraic problem size if compared with volumetric discretizations, especially in radiation problems. If Love's equivalence theorem is applied,[26] the NR's surface boundaries can be substituted with equivalent electric and magnetic surface currents that radiate in unbounded media according to the Stratton−Chu expressions, supported by the homogeneous Green's function as the integral kernel. By imposing the pertinent boundary conditions for the total electric and magnetic fields, a set of SIEs can then be derived with these surface currents as unknowns. In order to turn these SIEs discrete and render an algebraic linear system, these unknown currents are expanded in terms of divergence-conforming basis functions which are used as testing functions too (Galerkin MOM procedure), leading to a dense N × N matrix system of linear equations (wherein N would be the number of basis functions that expand the currents). Although this N × N matrix must compress so as to deal with large-scale electrodynamic problems,[25] there was no need to resort to acceleration techniques for the simulations in this paper, where the spectra are predicted for isolated particles only. The simulations were run on a workstation with a dual-processor configuration: 2 Intel Xeon E5420 microprocessors, each with 4 cores operating at a clock speed of 2.50

GHz. As for the dispersive dielectric permittivities of Au and Pd, their values were taken from the experimentally-retrieved data in Johnson and Christy.

***Refractive Index Sensitivity Measurements*:** Water-glycerol mixtures with a percentage of glycerol ranging from 0 to 80% v/v were used to change the refractive index of the Au and Au@Pd NRs. The refractive index of the different water-glycerol mixtures was calculated according to Lorentz–Lorentz equation:

$$\frac{n_{12}^2 - 1}{n_{12}^2 + 2} = \varphi_1 \frac{n_1^2 - 1}{n_1^2 + 2} + \varphi_2 \frac{n_2^2 - 1}{n_2^2 + 2}$$

Where n_{12} is the refractive index of the mixture, n_1 (1.33) and n_2 (1.47) are the refractive indices of water and glycerol, respectively, and φ_1 and φ_2 are their volume fractions.

Upon redispersion of the particles in different water-glycerol mixtures, the corresponding UV-vis-NIR spectra were recorded and the figure of merit calculated as the ratio between wavelength shift (at the maximum wavelength) and full width at half-maximum (fwhm)

***Hydrogen absorption-desorption measurements in Au@Pd NRs aqueous dispersions*:** Hydrogen absorption experiments were performed, at room temperature, using a 5mL flask capped with a sleeve stopper. A Teflon-coated magnetic stir bar was placed inside the flask to stir the solution during the hydrogen absorption experiment. A volume of 2.5mL of solution of Au@Pd nanorods solution was used for the experiment, after two centrifugation-redispersion cycles the particles were redispersed in half volume of initial solution. The air into the flask was removed with a vacuum pump until the solution began to bubble (typically 5 min). The hydrogen was introduced using a balloon filled with pure hydrogen by inserting a syringe-attached the balloon through a needle into the flask for 10 min under slow stirring to ensure a complete absorption. Under atmospheric pressure, hydrogen gas should fill the vacuum inside the flask, and the amount of dissolved hydrogen is considered the same as that under 1 atm pressure. Solubility of hydrogen in water at 30 ºC is 0.00147 g/kg water, or 1.47 ppm. After the H_2 absorption the UV–vis NIR absorption spectrum of the solution was recorded and afterwards the solution was strongly stirred for 1 min to remove the

absorbed hydrogen from nanoparticles. The nanocrystals were ready for next cycle of hydrogen incorporation and removal. The H2 absorption and desorption cycles were characterized by measuring the UV-Vis-NIR absorption spectrum in each step.

Hydrogen absorption-desorption measurements on gas phase*:* Optical gas sensing tests were performed by making optical absorption measurements over the wavelength range 350 nm < λ < 2000 nm using a Harrick gas flow cell coupled with a Jasco V-650 spectrophotometer. Samples deposited on SiO_2 glass substrates were exposed at room temperature to 1% v/v H_2 balanced in nitrogen, at a flow rate of 0.4 L/min. The substrate size was approximately 1 cm × 2 cm and the incident beam was normal to the film surface and covered a 9 mm × 1.5 mm area of the samples.

Au@Pd catalyzed 4-nitrophenol to 4-aminophenol reduction reaction under H_2 atmosphere**:** In a 1 cm path-length quartz cuvette, 2.0 ml of and aqueous Au@Pd dispersion. The air into the cuvette was removed with a vacuum pump and hydrogen was introduced by using a balloon filled with pure hydrogen as previously described. Finally, 13 µl of 4-nitrophenol water solution (0.05 mM final concentration) were added. A diode-array UV-visible-NIR spectrophotometer (Agilent 8453) was employed to monitor the reaction via time-resolved absorption spectra, which were recorded every 30 s, at room temperature. The 4-aminophenol product was identified by observing the changes in aborbance with time at 400 nm, where maximum changes in absorbance take place. The apparent observed rate constants k_{app} were calculated from plots of absorbance *vs.* time, using the first-order rate equation:

$$A_t = A_f + \Delta\alpha e^{-kt}$$

where A_t is the absorbance of the reaction mixture at time *t*, A_f is the final absorbance and *k* is the apparent observed first-order rate constant of the reaction.

Recyclability test. When the catalytic reduction of 4-NP to 4-AP was practically completed, 13 µl of 4-NP were added again to the reaction solution, and after mixing the solution the kinetic studies were continued. This procedure was repeated several times.

Time-Resolved kinetic SERS Measurements**:** For monitoring the catalytic reaction by SERS, first a self-assembled monolayer (SAM) of 4-NTP was adsorbed on the surface of

metal nanoparticles. In a typical reaction, 4 mL of an aqueous dispersion of Au@Pd nanoparticles (3.52 10^{10} particles mL^{-1}) were incubated with 40 µL of ethanolic solution of 10 mM 4-NTP overnight to form a saturated SAM on the nanoparticles surface. Then the nanoparticles were centrifuged (1735g-4000 rpm, 20 min and 2711 g-5000 rpm, 10 min for Au@Pd NRs and Au NRs, respectively) and redispersed in 4 mL of ultrapure H_2O. The nanoparticle-catalyzed 4-NTP to 4-ATP reduction was studied at room temperature upon addition of 10 µL of $NaBH_4$ to 1 mL Au NR or Au@Pd NR dispersion. The kinetics of the catalyzed reaction were measured in real time using time-resolved SERS. SERS experiments were conducted with a Renishaw InVia Reflex system. The spectrograph used a high-resolution grating (1200 grooves mm^{-1}) with additional band-pass filter optics, a confocal microscope, and a 2D-CCD camera. The SERS spectra were recorded from the solution phase with a 15x objective lens. The data were collected with an acquisition time of 10 s or 1 s for Au NR and Au@Pd NR, respectively. All samples were irradiated with a maximum power of 136 mW with a 785 nm excitation laser. Sequential spectra were collected during the reaction until completion of the reduction of 4-NTP into 4-ATP. We evaluated the catalytic activities of PTW and PTW@Pd nanoparticles at various $NaBH_4$ concentrations (25, 50 ,100 and 200 mM for PTW Au NRs and 0.5, 1, 5 and 10 mM for PTW Au@Pd NRs) and at different Au@Pd NR concentrations (7.04 10^{10}, 3.52 10^{10}, 1.76 10^{10}, 0.88 10^{10}, 0.59 10^{10} and 0.44 10^{10} particles mL^{-1}).

RESULTS AND DISCUSSION

Figure 1A shows the calculated extinction cross section spectra for Pd nanoparticles with different geometries; sphere, decahedron and pentatwinned nanorods with different aspect ratios. The simulations were performed using a numerical method based on the surface integral equation-method of moments (SIE-MoM) formulation (see Experimental Section for details).[24] Overall, all spectra are highly asymmetric due to an intrinsic Fano interference between LSPR and the interband continuum.[17] While Pd nanoshere and decahedron present the LSPR centered in the UV region, the optical response of PTW Pd nanorods (NRs) is strongly dependent on the aspect ratio of the particle, with a continuous red-shift from the UV to the NIR as the aspect ratio increases (similarly to Ag and Au nanorods).[6]

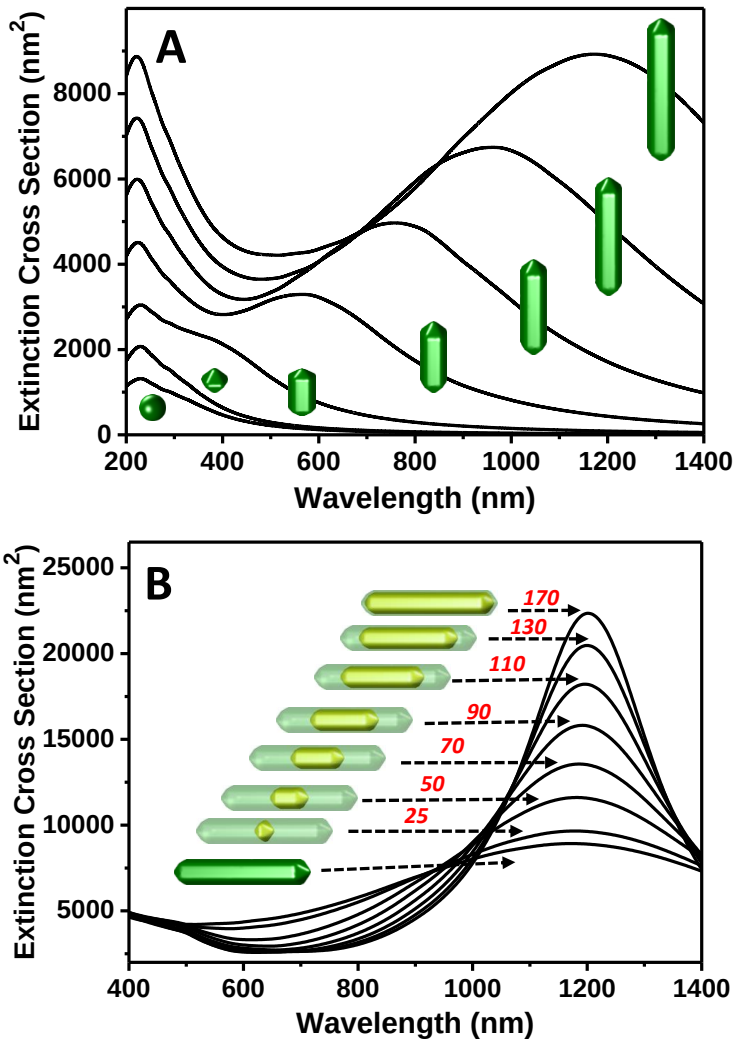

Figure 1. (A) Calculated extinction cross section spectra of pure Pd nanoparticles with different geometries in water; sphere (30 nm diameter), decahedra (30 nm diameter) and nanorods with dimensions 60x30, 90x30, 120x30, 150x30 and 180x30 nm. (B) Calculated extinction cross section spectra of Au@Pd nanorods with pentagonal cross-section. The overall dimensions are 180x30 nm, and the Au core presents a constant width of 25 nm and varying lengths from 25 nm to 170 nm. In the pictures the Au core is represented in yellow and the Pd shell in green. Values on the arrows indicate the assumed Au core length.

In addition, theoretical calculations of the optical response of PTW Pd NRs (180x30 nm) performed under polarized light, either perpendicular or parallel to the longitudinal axis, reveal two distinct modes: a transverse mode (located at 230 nm), and longitudinal mode (strongly dependent of the aspect ratio) corresponding to electron oscillations along or across their short and long axis, respectively (see Figure

S1 in Supporting Information, SI). As the aspect ratio of the NR increases (keeping the width of the nanorods constant), there is an increase in the red-shift and broadening of the longitudinal LSPR band. Taking into account these theoretical calculations, one would need to fabricate Pd NRs with aspect ratios higher than 4 to obtain particles with optical responses in the NIR region. Besides, the calculated spectra clearly show that pure Pd NRs exhibit broad LSPR responses, which could be a limiting factor for LSPR-based sensing. Recently, Jung et al. and Chen et al. synthesized long Pd NRs by potentiostatic electrochemical deposition employing an anodized aluminum oxide template[27] and a seed-mediated synthesis,[6] although they demonstrate the tuning of the LSPR as a function of the aspect ratio, the optical response of the fabricated NPs was rather poor. The origin of the relatively poor optical response of Pd nanorods is, in part, due to the large imaginary part of the Pd dielectric function which results in a broadening of the LSPR band.

Alternatively, we have performed theoretical calculations on PTW Au@Pd core-shell nanorods with overall dimensions of 180x30 nm, but varying the length of Au NR from 25 nm to 170 nm with a constant width of 25 nm. The results show that increasing the amount of Au present in the core leads to a significant improvement of the optical response of the Au@Pd nanorods over pure Pd NRs in terms of longitudinal LSPR band intensity and plasmon line width without affecting its peak maxima (see Figure 1B). These results clearly suggest that Au NR supports boost the optical response of Au@Pd NRs while maintaining pure Pd like surface properties. Taking into account that: (1) LSPR linewidth is inversely proportional to the coherence time of the free conduction band electrons,[28] and (2) Au nanoparticles exhibit long coherence time, the optical improvement could be explained in terms of the overall increase of coherence time due to the presence of a gold core. Therefore, designing Pd nanoparticles with Au@Pd core-shell type morphology would provide novel alternative materials for plasmonic applications. On the other hand the combination of the Pd with Au could also improve the performance in plasmon-mediated chemical reactions (since the absorption is its main contribution to the total extinction of Pd NPs)[16] or in photothermal therapy of cancer (Pd exhibits better photothermal stability that Au).[29,30]

Inspired by the interesting results obtained from the theoretical calculations, here we proposed to obtain Pd nanoparticles with narrow and tunable optical responses in the NIR region employing a seeded growth strategy with PTW Au NRs as seeds. Typically, Au nanorods were 114.6 ± 8.1 nm long and 26.3 ± 2.4 nm wide (aspect ratio of 4.4) and the longitudinal LSPR band was centered around 930 nm.[23] The overgrowth of Pd on Au NR surface was carried out in a controlled manner through the reduction of Pd^{2+} salt under mild conditions, using ascorbic acid as reducing agent and CTAB or CTAC as capping agent.[31] Figure 2 shows the spectral evolution during the overgrowth of Pd on Au nanorod seeds in the presence of CTAB (Figure 2A) and CTAC (Figure 2B) at 30 ºC. The absorption band centered at 340 nm corresponds to the Pd ions (CTTS, charge transfer to solvent) and its time evolution allowed us to follow the reduction of the Pd precursor. Moreover, the spectral evolution of the longitudinal LSPR band of the Au NRs upon Pd deposition in the presence of CTAB and CTAC surfactants shows that the nature of the surfactant counter ion clearly influenced the Pd overgrowth. In the presence of bromide ions the Pd reduction gave rise to an initial damping in the optical response followed by a gradual and continuous red-shift in the position of the longitudinal LSPR band, together with an increase in intensity, till the total consumption of the Pd ions (Figure 2A). Conversely, the presence of chloride ions during the Pd deposition led to a continuous damping of the longitudinal LSPR band accompanied by an initial red-shift and a subsequent blue-shit in its position (Figure 2B). Summarizing, the presence of bromide ions lead to the production of Au@Pd hererostructures with an intense LSPR band centered at 1215 nm, while in the presence chloride ions the optical properties displayed a low intense and broad band centered at ca. 950 nm.

In order to clarify the origin of the different optical evolution observed in the overgrowth of Pd in CTAB and CTAC, the resulting nanoparticles were characterized by transmission electron microscopy (TEM). Figures 2D-F and S2 in SI show representative TEM images of the Au NRs before (Figure 2E) and after the Pd deposition in the presence of either CTAB (Figure 2D) or CTAC (Figure 2F). As depicted in Figure 2C, in the presence of CTAB, the Pd salt reduction takes place preferentially on the tips of the Au NRs leading to an increase of overall aspect ratio from 4.4 (initial Au NRs) to 6.2

(Au@Pd NRs, average length and width of 189.6 ± 44.9 nm 30.9 ± 4.4 nm, respectively). On the other hand, in CTAC the formation of a rough/dendritic Pd shell on the entire Au NRs surface is observed (see Figure 2C) and thus results in a decrease of aspect ratio from 4.4 to 3.1 (average length and width of 134.0 ± 12.7 nm and 43.5 ± 4.5 nm, respectively). Since CTAB and CTAC have the same hydrophobic group, the difference in the Pd growth process could be attributed to their counter ions, Br^- and Cl^-, respectively.

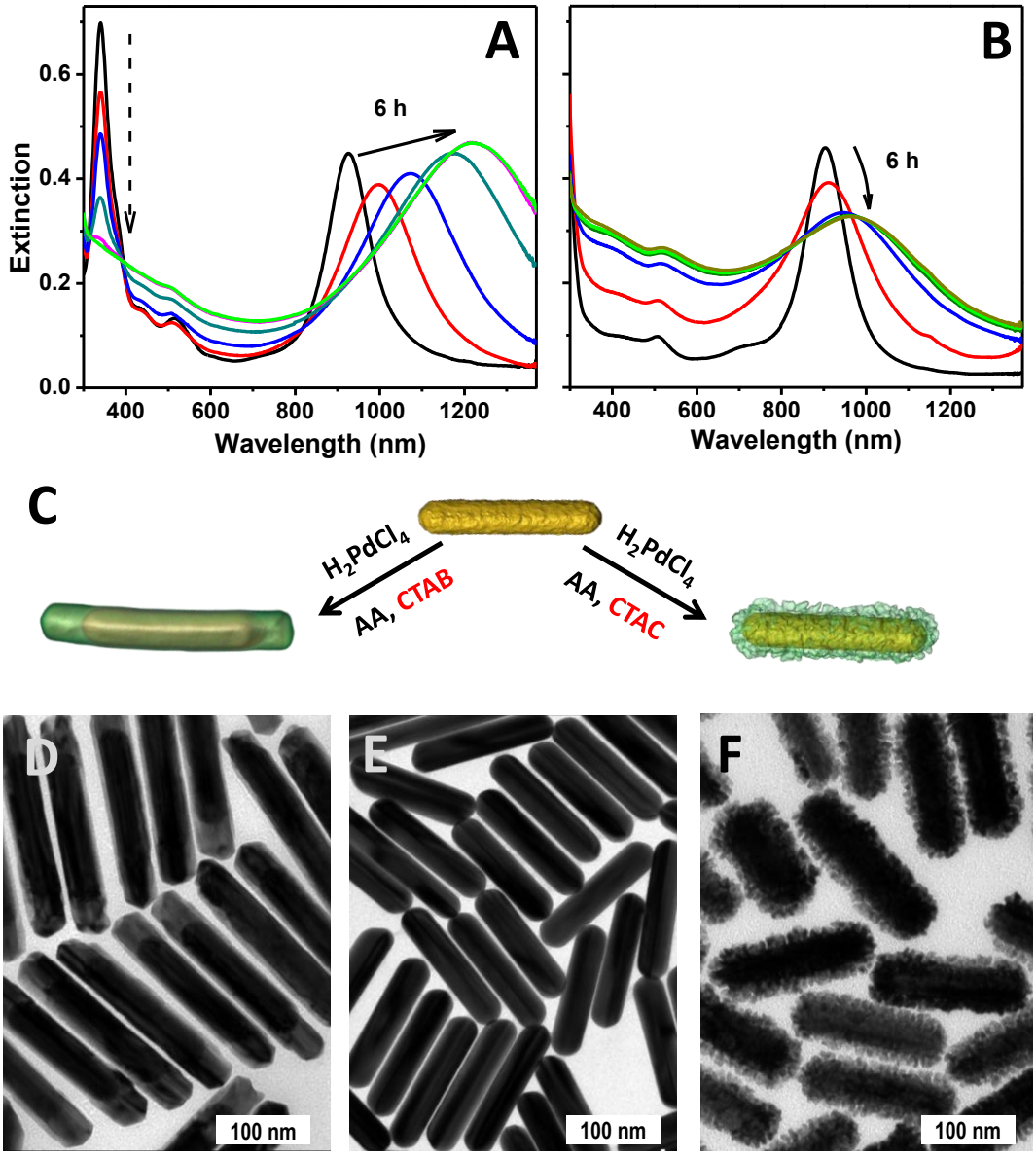

Figure 2. (A-B) Time evolution of the UV-visible-NIR extinction spectra during the overgrowth of PTW Au nanorods with Pd in the presence of CTAB (A) or CTAC (B). (C-E) Representative

TEM images of the original PTW Au nanorods before (E) and after the deposition of Pd in the presence of CTAB (D) and CTAC (F).

Moreover, as observed in Figure 2A, the overgrowth with Pd in the presence of bromide ions enabled to tune the longitudinal LSPR band across the NIR region by reaction time. Alternatively, such control can be easily achieved by varying the concentration of Pd salt while keeping the constant amount of Au NR seeds. As shown in Figure 3, the LSPR band progressively red-shifts from 930 nm (original PTW Au NRs) to ca. 1300 nm as the concentration of Pd salt in the growth solution increases from 0 to 117 μM. Interestingly, it should be pointed out it is also accompanied with a broadening of the LSPR band due to the increase of the imaginary part of Pd dielectric function at longer wavelengths (see Figure S3 in SI). However, the spectra appears much narrower compared to extinction spectra of pure Pd NRs, which is in agreement with theoretical calculations (Figure 1). High-angle annular dark field scanning TEM (HAADF-STEM) analysis of the final products (see Figure 3) clearly shows the increase in aspect ratio of the nanoparticles with the increase of Pd concentration. Since HAADF-STEM images yield intensities that scale with the atomic number Z, the palladium shells can be easily discerned from the gold cores (brighter in the dark field images) unlike in TEM images, where the contrast difference between two elements (Au & Pd) is not clear (Figure 2D). The average length of the NRs increases with the concentration of Pd salt precursor while the width remained almost constant (see Figure S4 in SI), evidencing a preferential Pd deposition on the tips. In all cases, the kinetics of the reduction process can be speed up by increasing the temperature without affecting the spectral evolution and consequently the final products. In fact, experiments performed in the presence of CTAB at 70 ºC finished in less than 30 min obtaining similar results (see Figure S5 in SI), suggesting the possibilities of large scale production. Similar results at higher temperatures rules out any kinetic effect in the preferential deposition of palladium at the PTW Au nanorods.

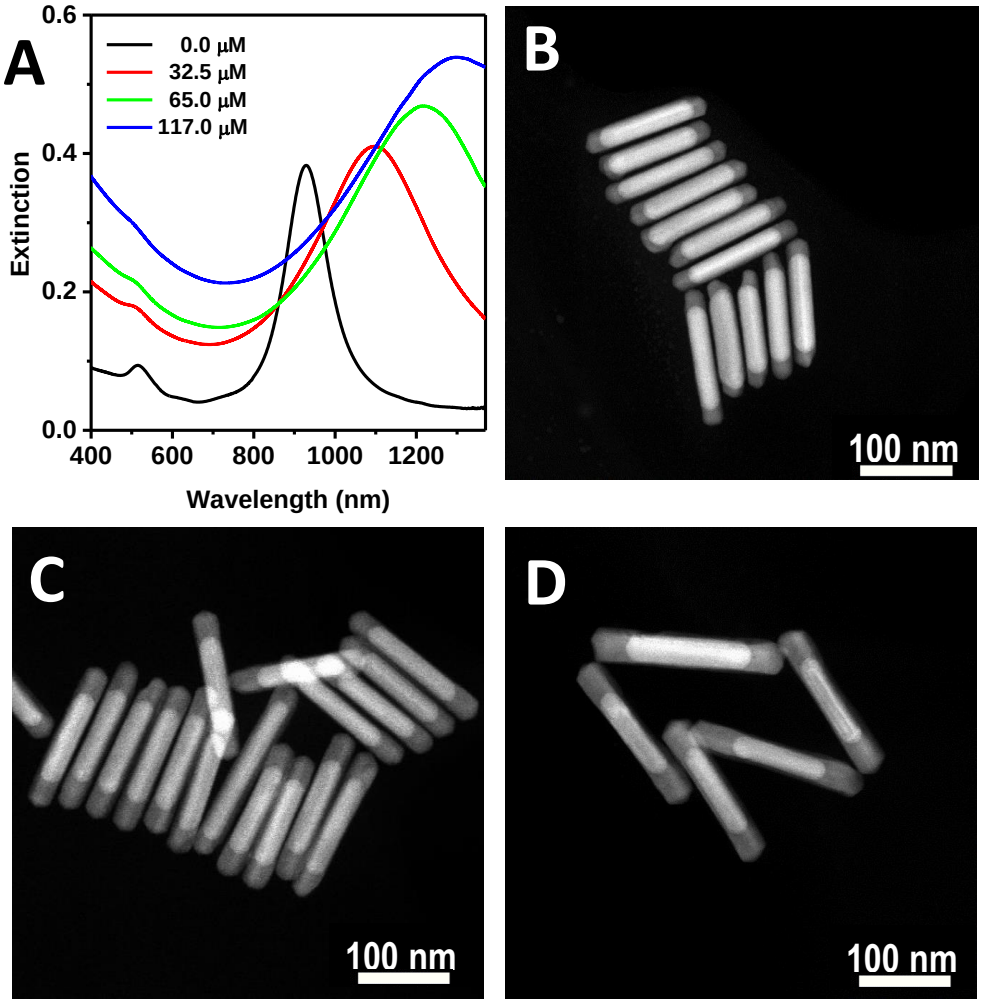

Figure 3. (A) Visible-NIR extinction spectra of PTW Au nanorod used as seeds (black line) and Au@Pd nanorods overgrown with different Pd salt concentrations, as indicated. (B-D) Representative HAADF-STEM images of the Au@Pd nanorods overgrown with different Pd salt concentration, 32.5 μM (B), 65.0 μM (C) and 117.0 μM (D).

Furthermore, the extinction spectra of the Au NR seeds, as well as the resulting Au@Pd nanorods, have been simulated using a numerical method based on SIE-MoM formulation (see Experimental Section for details).[24] For the calculations, we considered as model a nanorod with a pentagonal cross section and with hemidecahedral end cups. The dimensions were taken from the size distribution histograms resulting of the TEM analysis of samples showed in Figure S4. As can be clearly seen in Figure S6 in SI, the experimental extinction spectra of all samples are in excellent agreement with the theoretical spectra obtained from calculations.

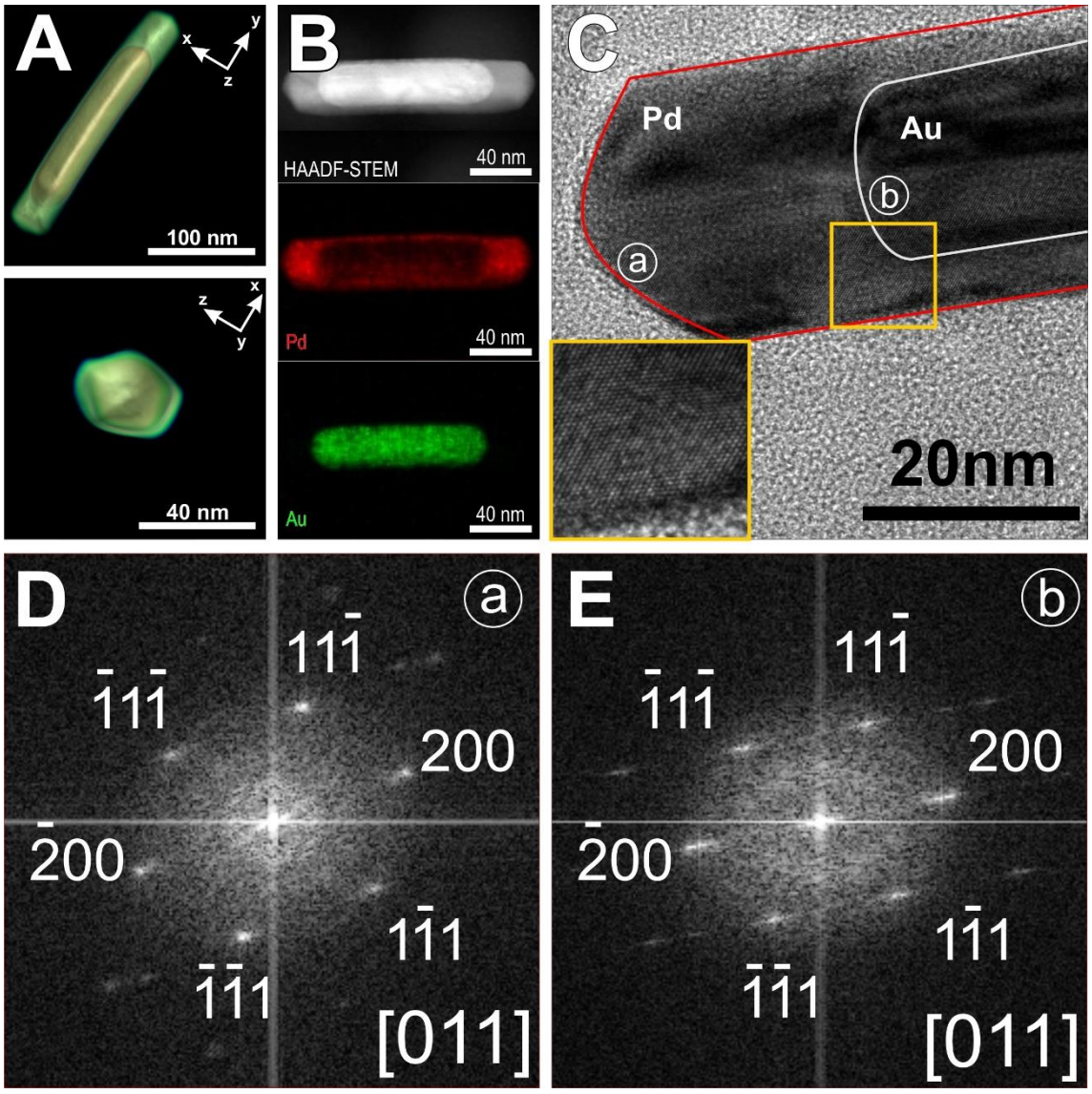

Figure 4. (A, B) Electron tomography 3D reconstruction and XEDS elemental maps of a single PTW Au@Pd NR. (C) HR-TEM image showing the external Pd shell covering the central Au core. (D, E) FFT patterns corresponding to the areas "a" and "b" in C.

Although previous reports have demonstrated the epitaxial deposition of Pd on Au surfaces,[32] the influence of the halide ions of the surfactants on the directional overgrowth of Pd shell has not been observed. In order gain deeper insights of the Pd overgrowth and the role of Br^- and Cl^- ions, both types of obtained Au@Pd heteronanostructures were further analyzed by electron tomography, Energy-Dispersive X-ray Spectroscopy (XEDS) and electron diffraction. Three-dimensional (3D) reconstruction and the XEDS analysis of a single Au@Pd NR are shown in Figures 4A

and 4B, respectively. The external Pd shell with a pentatwinned cross section can be clearly visualized from the 3D reconstruction, suggesting that the crystallinity preserves after the overgrowth of Pd shell. In the presence of CTAB, a preferential deposition of Pd on the {111} tip facets of the PTW Au NR can be observed, although a thin Pd layer is also formed on the {100} lateral facets, which can be further confirmed by XEDS as well. Besides, the elemental mapping does not show any possible alloying between Pd and Au. Detailed information about the Pd growth was obtained by studying the FFT pattern of a PTW NR at the tip (point "a" in Figure 4C), where only Pd is present, and in the central area (point "b"), where Au and Pd are both present. The electron diffraction analysis (Figure 4D, E) reveals that the spots of the FFT patterns of these two areas coincide, which suggests the epitaxial growth of Pd on Au. In addition, the FFT patterns indicate the lattice strain (pronounced in Figure 4E) as well as twinning of the rod. Finally, the FFT patterns also reveal that these PTW Au@Pd NRs are oriented in both ⟨110⟩ and ⟨111⟩ zone axes, which have been reported to be the main possible orientations with respect to the electron beam for PTW NRs.[33]

As already discussed above, when CTAC was used as surfactant in place of CTAB, a uniform rough Pd shell surrounding the Au core was observed. This can be clearly seen by HAADF-STEM and electron tomography (Figure 5A), which is in accordance with the data obtained from the low resolution TEM (see Figure 2E). As shown in Figure 5A, electron tomography provides a clear 3D visualization of thin dendritic Pd shell on Au NR surface. The FFT patterns relative to the Au@Pd and the pure Pd shell shown in Figures 5B and C confirm that epitaxial growth of Pd on Au as both the patterns appears to be same.

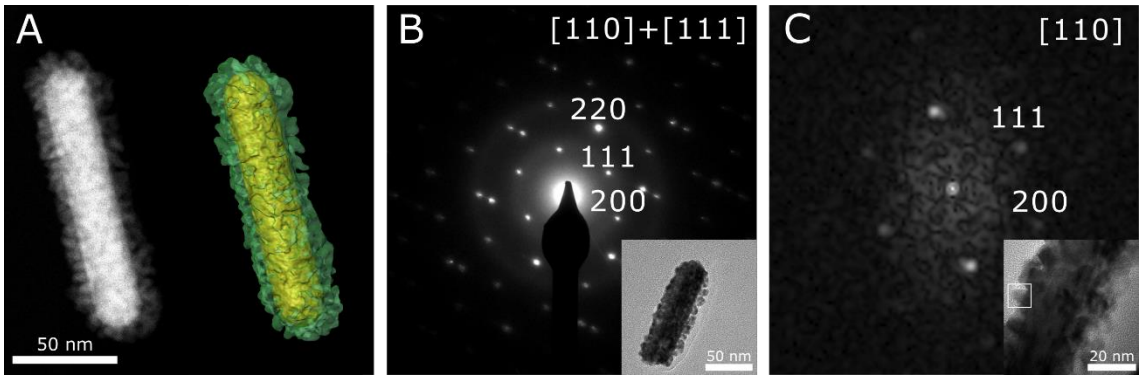

Figure 5. (A) HAADF-STEM picture and 3D tomographic reconstruction of a single Au@Pd NR when the overgrowth is performed in the presence of CTAC. (B, C) HR-TEM images with the corresponding FFT patterns.

Growth Mechanism. So far we have demonstrated the presence of either CTAB or CTAC in the reaction media led to Au@Pd nanoparticles with different morphologies, implying two different growth modes. In order to propose a growth mechanism that explains the different behavior observed for both surfactants, we have to take into account that; *i*) the initial gold NRs are enclosed by 5 {100} lateral facets and the tips by 5 {111} facets,[34] *ii*) the interactions between halide ions and noble metals increase in the order $Cl^- < Br^- < I^-$,[35] *iii*) previous reports have evidenced the preferential binding of halide to the {100} facets of various metals inhibiting its growth,[36] *iv*) the lattice mismatch (5%) between Au and Pd is low enough to allow epitaxial growth, *v*) the growth mode will be mainly determined by the ratio between the rates of Pd atom deposition and surface diffusion[20] and *vi*) the temperature is not a key parameter determining the growth mode. Bearing all these factors in mind, the lack of intrinsic differences between Au and Pd in terms of lattice constant and cohesive energies should induced a layer by layer (or Frank-van der Merwe) Pd growth on the {100} and {111} Au facets at the initial stages of the reaction.[37] Conversely, when the growth takes place in the presence of CTAB, bromide ions will be preferentially adsorbed to the {100} lateral facets of the NRs. According to the collision model,[37,38] the Pd deposition can be suppressed on those facets, while is promoted on the tips enclosed by five {111} facets leading in this case to an increase in the overall aspect ratio.[36,39] On the other hand, in the absence of tightly adsorbed bromide ions a sort of layer plus

island growth (Stranski-Krastanov mode) is most likely observed. The loosely adsorbed chloride ions could not hinder the Pd deposition in the lateral facets of the Au NR.[35] Therefore, the newly formed Pd atoms can be deposited on the entire surface of the Au NR and then evenly distributed along the {100} and {111} facets. Although this could initially lead to a homogenous deposition, the high activation energy barrier for the diffusion of Pd adatoms on (100) causes the Pd atoms to stay and accumulate on the newly formed nucleation sites resulting in a dendritic or island growth mode. In summary, the presence of bromide ions and their interaction with the {100} facets will lead to thermodynamically controlled growth, as opposed to kinetically controlled, resulting in preferential deposition at the nanoparticle tips.

Refractive index sensitivity of PTW Au@Pd nanorods. The enhanced plasmonic responses of Au@Pd NRs in the NIR region with narrow line width inspired us to investigate their refractive index sensitivity by both theory and experiment in order to evaluate their potential applicability in LSPR based sensing. The position of the LSPR band is also very important in terms of sensitivity, since a more red-shifted LSPR band will led to a higher refractive index sensitivity.[22] Recently, some authors claim as key parameter controlling the sensitivity of plasmonic nanoparticles the aspect ratio.[14] Therefore, for a better comparison, we calculated the influence of the refractive index on the extinction cross section for a single PTW NR of pure Au, pure Pd and core-shell Au@Pd, having similar overall dimensions (aspect ratio) and the longitudinal LSPR band centered at 1100 nm water (Figure S7 in SI). The plot of the theoretical longitudinal LSPR shift *vs* the refractive index of the surrounding medium shows, in all cases, a linear relationship (see Figure 6A).[40] Besides, the refractive index sensitivity was determined from the slopes of the linear fit. The results indicates that PTW Pd NRs (1213 nm/RIU) exhibit higher refractive index sensitivity than Au@Pd NR (877 nm/RIU) and Au NR (741 nm/RIU). It indicates that the composition is also a parameter affecting the refractive index sensitivity. Nevertheless, it should be pointed out that pure Au NRs exhibit a better sensitivity in terms of FOM.[41] The calculated FOM for Pd, Au@Pd and Au nanorods with the LSPR band centered at 1100 nm is 1.4, 2.5 and 8.1, respectively. The theoretical data indicate that Au@Pd NRs exhibit higher extinction and better FOM compared to pure Pd NRs.

Experimental bulk refractive index sensitivity measurements were performed with PTW Au@Pd NRs with LSPR centered at 1034 and 1197 nm by dispersing them into different volume ratios of water-glycerol mixtures (see spectra and average dimensions in Figure S8 in SI). The refractive index of the solvent mixtures was calculated according to the Lorentz-Lorenz model.[42] Figure 6B shows the linear dependence of LSPR shift *vs* refractive index for both samples, the refractive index sensitivity obtained from the linear fit were 719 and 1062 nm/RIU for PTW Au@Pd NRs with the longitudinal LSPR band located at 1034 and 1197 nm, respectively. As expected, the sample with longer LSPR presented higher sensitivity. Additionally, we compared the refractive index sensitivity of PTW Au@Pd NRs obtained in the present work with those determined previously by others for plasmonic nanoparticles with arbitrary shapes (see Table S1 in SI and ref. ([14])). It is clear that the PTW Au@Pd have the highest sensitivity factor among all Pd based bimetallic nanoparticles reported to date.[16,43,44] Moreover, the refractive index sensitivity of these Au@Pd NRs are even higher than that reported for other highly sensitive Au/Ag nanoparticles (nanopyramids,[22,45] nanoprism,[46] nanorings,[47] nanoframes,[48] etc..). Thus, to the best of our knowledge the bulk sensitivity of 1062 nm/RIU observed for PTW Au@Pd NRs with the longitudinal LSPR band located at 1197 nm is one of the highest reported for a nanoparticle system, being comparable to that reported for Ag nanoplates.[49] Additionally, we have also investigated the dependence of nanoparticle refractive index sensitivity of these Au@Pd NRs on their LSPR wavelength in comparison with the reported literature for Au, Ag and Au@Pd of various morphologies (see Figure S9 in SI). The graph evidences that the Au@Pd NRs present one of the highest refractive index sensitivity comparable to that showed by Ag nanoplates. Nevertheless, the broadness of the LSPR band due to the large imaginary part of the dielectric constant gives rise to moderate FOM of 2.2 and 2.4, see Table S1 in SI and ref ([14]), values lower than those reported for Au or Au@Ag bipyramids.

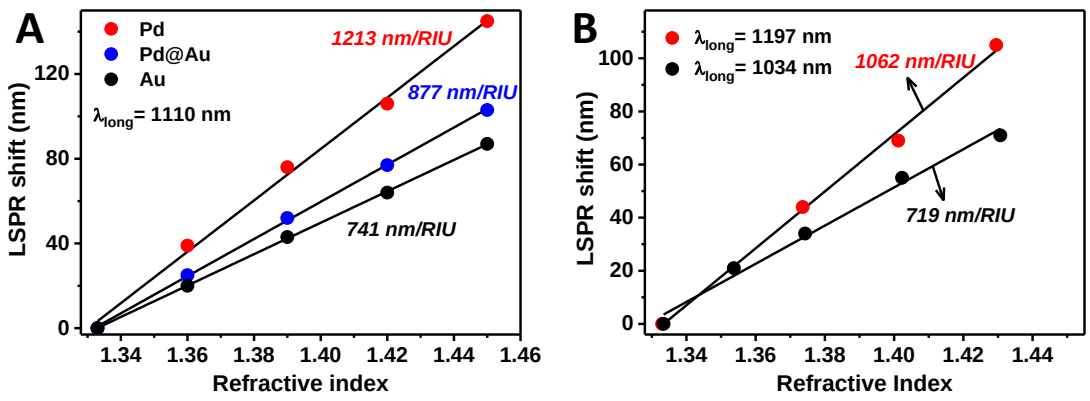

Figure 6. (A) Calculated dependences of the longitudinal LSPR shift on refractive index changes for a single PTW NR of pure Au, pure Pd and core-shell Au@Pd with the longitudinal LSPR centered at 1100 nm (B) Experimentally obtained dependences of the longitudinal LSPR shift on refractive index changes for PTW Au@Pd NRs with LSPR centered at 1197 and 1034 nm in water.

Optical sensing of Hydrogen using PTW Au@Pd NRs. Generally, when H_2 exposed to Pd, molecular hydrogen dissociates and atomic hydrogen diffuses into the Pd surface resulting in the formation of palladium hydride (PdH_X, being x the ratio of H to Pd in the lattice). Consequently, the density of electronic states at the Fermi level decreases, electrons from hydrogen atom enters the s - and d - bands of Pd,[50] which causes change of the dielectric function and therefore a red-shift of the LSPR and a slight decrease of its intensity.[21] Thus, plasmonic NPs could be used for optical sensing of hydrogen. Plasmonic based sensors constitute an alternative to the electrical sensors, which are limited by the possible generation of sparks. Therefore, we studied the ability of PTW Au@Pd nanorods for optical detection of hydrogen either dissolved in water or in gas phase. The former was performed by introducing hydrogen gas from a balloon through a syringe into a flask containing Au@Pd NRs (see Experimental Section for details). The concentration of hydrogen in water was 1.47 ppm, which corresponds to the dissolved hydrogen in water at 1 atm. As shown in Figures 7A and 7B, the exposure of hydrogen gas dissolved in the solution leads to a fast (in seconds) and remarkable red-shift of the longitudinal and transverse LSPR of the Au@Pd NRs. Thus, PTW Au@Pd NRs with longitudinal LSPR band at ca. 1010 nm underwent a red-shift of 42 nm, while ca. 27 nm red-shift was observed for the transverse LSPR band (Figure

7B). We then tested the spectral reversibility of PTW Au@Pd NRs by hydrogen absorption-desorption cycles. As previously reported,[44] once PdH_X is formed, the hydrogen can be removed by shaking the colloidal solution for a min, thus result in a blue shift of the LSPR. As depicted in Figure 7C, the longitudinal LSPR shift *vs* absorption-desorption cycles reveals the reversible behavior. The LSPR almost returns to its starting spectral position even after 6 cycles. The performance of the PTW Au@Pd NRs for spectral sensing of dissolved hydrogen is similar to that shown for Au@Pd core–shell tetrahexahedral, octahedral, and cubic nanocrystals recently.[44]

In addition, the hydrogen detection in gas phase was also investigated using PTW Au@Pd NRs deposited on a glass substrate (see Experimental Section for details). As showed in the inset of Figure 7D and S10 in SI, the NRs are uniformly distributed and most of them spatially isolated from neighboring NRs. Before using the Au@Pd NR substrates for H_2 sensing, the sensing platform was first treated with O_2 plasma to remove the PVP from the nanoparticles surface which can hinder the particles sensitivity. In order to perform the hydrogen sensing study, the extinction spectra of the PTW Au@Pd NRs platform was recorded during three absorption-desorption cycles using a hydrogen-nitrogen gas mixture with 1% hydrogen (see Experimental Section for details). Figure 7 shows the longitudinal LSPR of the PTW Au@Pd NRs platform at 0% and 1% of hydrogen for three consecutive cycles, in which the observed plasmon shift is around 38 nm. In the second and third cycles the plasmonic behavior is almost identical while the first cycle is slightly different. After two cycles of H_2 absorption and desorption, the spectra of these single NCs did not return to their starting spectral positions. This hysteresis in the LSPR is attributed to the residual H atoms on the subsurface sites of Pd which cannot be removed at RT. We found that the performance of the PTW Au@Pd NRs platform is comparable to the largest value reported up to day at 1% hydrogen under similar conditions.[21]

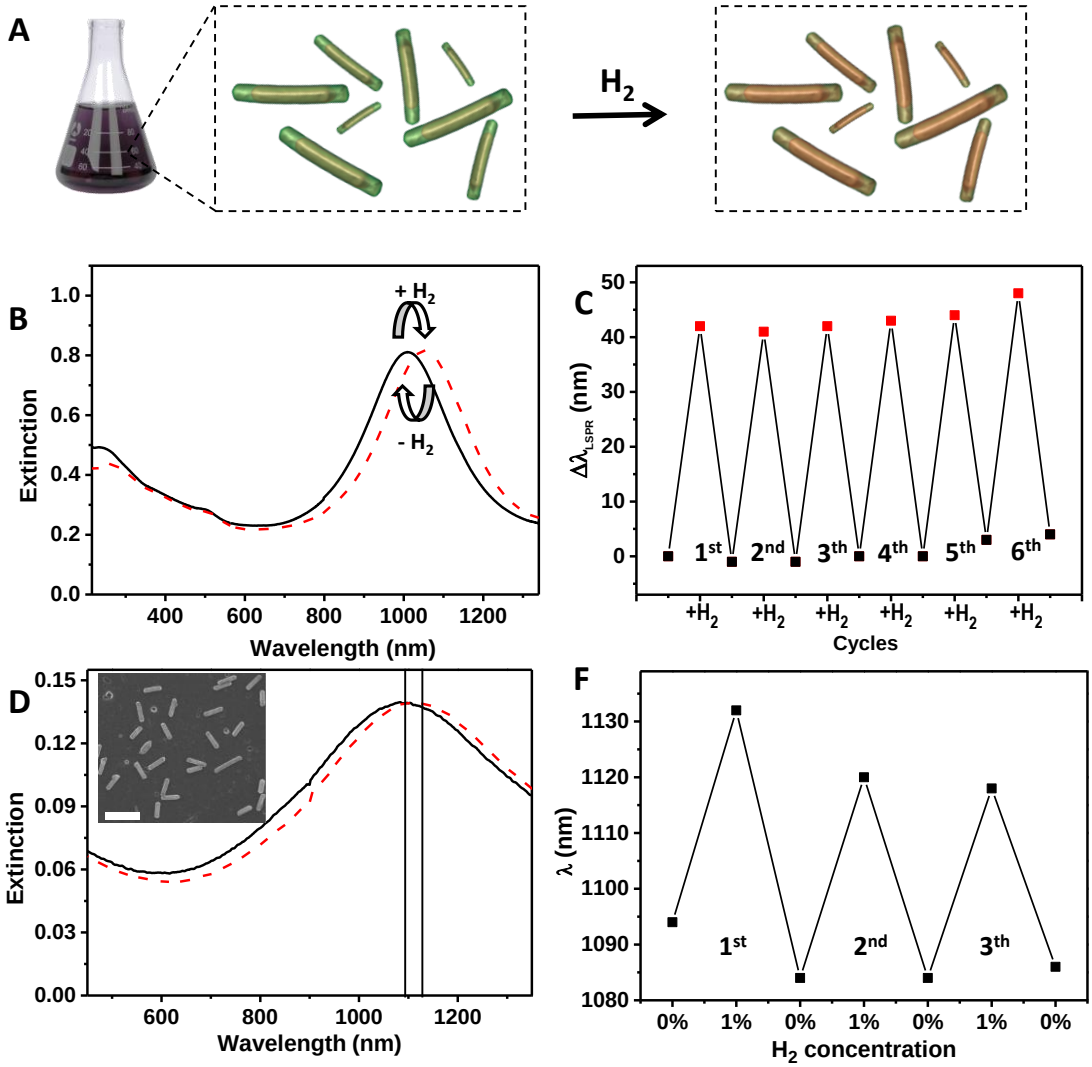

Figure 7. (A) Schematic representation of the palladium hydride formation after exposing an aqueous dispersion of Au@Pd NRs to hydrogen. (B) Evolution of the extinction spectra of PTW Au@Pd NRs during the exposition to 1.47 ppm of hydrogen gas dissolved in the aqueous colloidal dispersion. (C) Longitudinal LSPR shift of an Au@Pd NRs aqueous colloidal dispersion during different hydrogen absorption-desorption cycles. (D) Evolution of the extinction spectra of PTW Au@Pd NRs on glass during the exposition to 1% of hydrogen gas. (F) Longitudinal LSPR shift of Au@Pd NRs deposited on glass during different 1% hydrogen cycles.

Optical monitoring of reaction progress by SERS: It is well known that Pd NPs are excellent candidates for catalysis, however, coupling them with Au NRs would make them multifunctional, thus useful for optical monitoring of catalytic reactions. To gain insight into the catalytic activity of the optically active Au@Pd nanoparticles, we selected the hydrogenation of 4-nitrophenol (4-NP) as model reaction, which has been

widely used for the evaluation of the catalytic activity of noble metal nanoparticles.[51] Initially, considering the absorption capabilities of the Au@Pd NRs towards hydrogen, we decided to test the recyclability towards the hydrogen-mediated reduction of p-nitrophenol in water. This reaction can be easily monitored by UV-visible spectroscopy, since nitrophenolate ions and 4-aminophenol (4-AP) display absorption bands centered at 400 nm and 300 nm, respectively. Figure S11 in the Supporting Information shows the reaction kinetics plotting the absorption intensity at 400 nm *vs.* reaction time for the reduction of 4-NP in water under a H_2 atmosphere (1 atm) at room temperature. The concentration of dissolved hydrogen in water at 1 atm and 25 ºC is 1.47 ppm,[44] which can be considered as constant allowing us to treat the kinetics of the catalytic process as a pseudo-first order reaction. To check the reproducibility/reusability of the Au@Pd nanorods as catalysts, the nitro to amine conversion was repeated several times through sequential addition of 4-NP to an aqueous dispersion of Au@Pd nanoparticles under a H_2 atmosphere. The consistency of the observed pseudo-first order rate constant, k_{obs}, between the first and fifth additions of 4-NP (2.20×10^{-3} s^{-1}, 1.94×10^{-3} s^{-1}, 2.36×10^{-3} s^{-1}, 1.84×10^{-3} s^{-1}, 1.54×10^{-3} s^{-1}, respectively) is a clear evidence for the stability and reusability of the Au@Pd catalyst (see Figure S11 in SI).

UV-visible absorption spectroscopy only provides information about the overall reaction kinetics, but the nice optical properties of the Au@Pd nanoparticles allowed us to go in depth the intrinsic kinetics and mechanism of the surface-catalyzed reaction through time-resolved SERS measurements. Au@Pd nanorods with LSPR band centered at 960 nmwere chosen as plasmonic SERS platform. As model reaction the catalytic conversion of 4-nitrothiophenol (4-NTP) into 4-aminothiophenol (4-ATP) was selected (Figure 8A). 4-NTP was preadsorbed on the NRs surface through the thiol group forming a self-assembled monolayer. Analyzing the SERS signals from the molecules adsorbed on the surfaces of freestanding nanoparticles, we were able to study the reaction kinetics as a function of the reactant (4-NTP) or the product (4-ATP). The fact that 4-NTP was absorbed on the catalyst surface allowed us to study the intrinsic kinetics avoiding interference related with the adsorption and desorption of the reactants and products. The SERS spectrum of 4-NTP has two well-defined

characteristic vibrational bands at 1330 cm^{-1} and 1570 cm^{-1}, corresponding to the O–N=O symmetric stretching and phenyl ring stretching modes, respectively (Figure 8B). After the addition of $NaBH_4$ the peak intensities at 1330 and 1570 cm^{-1} were observed to gradually decrease while a new peak, assigned to the phenyl ring of 4-ATP, showed up at 1593 cm^{-1}, see Figure 8B. The vibrational modes observed in SERS correlate well with the bands measured in Raman for 4-NTP and 4-ATP.[52] It should be pointed out that the catalytic reaction did not alter the stability of the Au@Pd colloids, as evidenced by their extinction spectra (see Figure S12 in SI). The catalytic hydrogenation of 4-NTP can be considered a two-step consecutive reaction either *via* direct route with a hydroxylamine intermediate (see Figure 8A) or via a condensation route with the formation of an azo compound (4,4'-dimercaptoazobenzene, DMAB).[53] Different authors have identified DMAB as a transient intermediate along the reaction pathway when the reaction was catalyzed by metal nanoparticles in colloidal dispersions.[54,55] In our experiments we did not observe the formation of intermediates such as hydroxylamine or dimercaptoazo benzene (see SERS spectra in Figure 8B), suggesting that in the present case the intermediate reacted very fast and therefore it could not be detected.

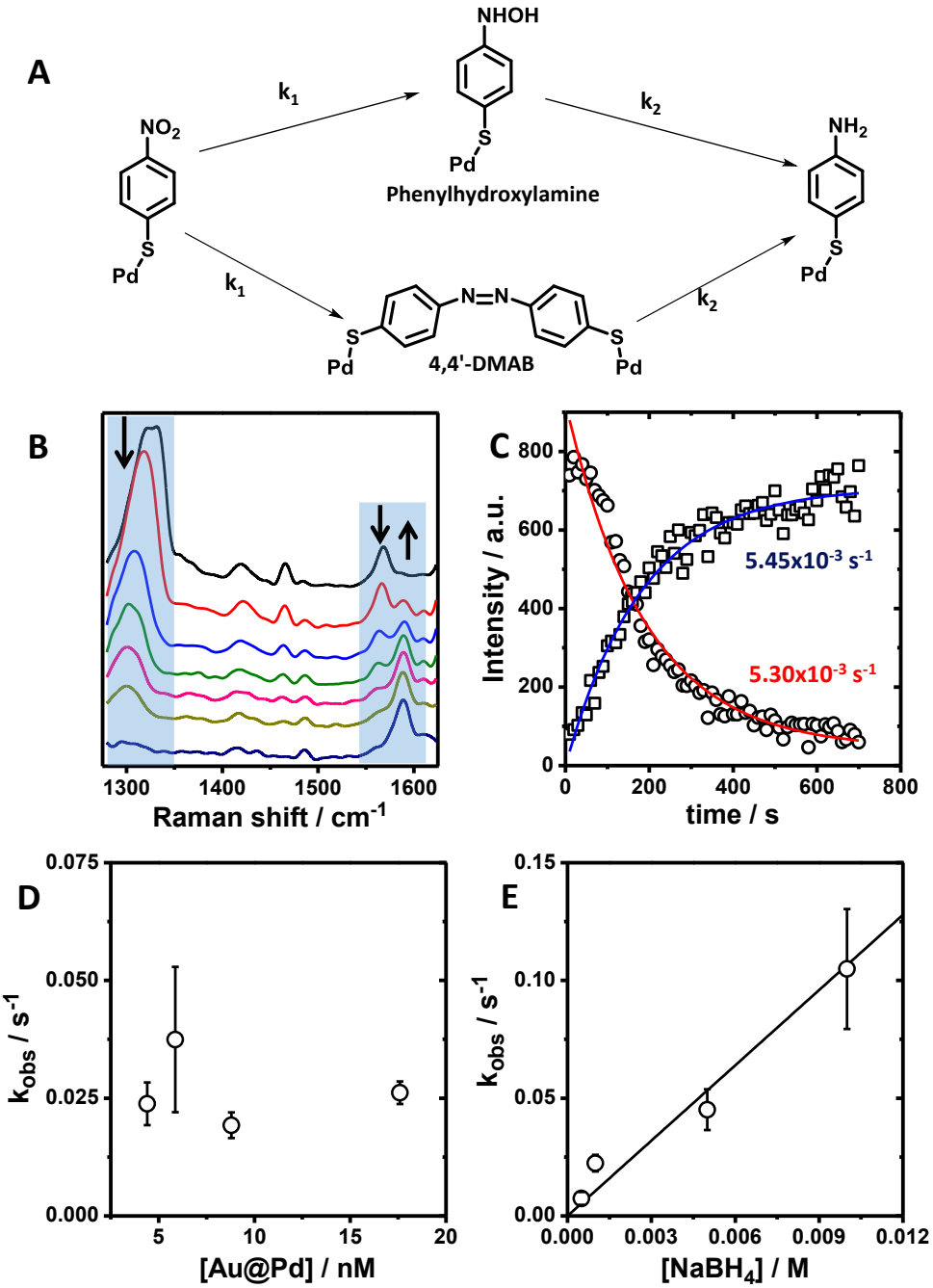

Figure 8. (A) Reaction pathways for the nitro to amine (aniline) conversion; a direct route via a hydroxylamine intermediate or a condensation route via the formation of 4,4'-dimercaptoazobenzene, 4,4'-DMAB. (B) Representative SERS spectra measured at different reaction times. [Au@Pd]= 9 nM, [$NaBH_4$]= 5 mM. (C) Kinetic trace of the SERS intensities at 1570 cm^{-1} (4-NTP) and at 1593 cm^{-1} (4-ATP). The lines represent the best fit of a first order equation to the experimental data, [Au@Pd]= 9 nM and [$NaBH_4$]= 2 mM. (D) Observed pseudo-first order rate constant as a function of the Au@Pd nanoparticle concentration, [$NaBH_4$]= 2 mM. (E) Influence of $NaBH_4$ concentration on the kinetics of hydrogenation of 4-NTP adsorbed on Au@Pd nanoparticles, [Au@Pd]= 9 nM. T= 25 ºC in all cases.

The catalysis was carried out in a large excess of $NaBH_4$ compared to 4-NTP, it allowed treating the reaction kinetics for the first reaction step of the reaction (the disappearance of 4-NTP) as a pseudo-first order reaction (see equation 1).

$$\frac{[4-NTP]_t}{[4-NTP]_o} = e^{-k_1 t} \qquad (1)$$

where k_1 represents the rate constant of the disappearance of 4-NTP, the subscripts *o* and *t* denote the initial concentration and the concentration at a given time *t* of 4-NTP, respectively. For clarity equation 1 has been expressed in terms of reactant and product fraction.

Besides, the rate equation for the formation of 4-ATP would follows a double exponential (see equation 2).

$$[4-ATP]_t = [4-NTP]_o - [4-NTP]_o e^{-k_1 t} - \left(\frac{k_1}{k_2 - k_1}\right)[4-NTP]_o\left(e^{-k_1 t} - e^{-k_2 t}\right) \qquad (2)$$

where k_2 represent the rate constant of the disappearance of 4-NTP, the subscripts *o* and *t* denote the initial concentration and that at a given time *t* of 4-NTP or 4-ATP, respectively.

Additionally, the fast reaction of the intermediate indicated that the reaction rate of the second step (k_2) was larger than the first one (k_1) which allowed us to apply the steady-state approximation and therefore the formation of the intermediate should be the rate determining step. If the concentration of the intermediate remained very low along the reaction process and considering $k_2 >> k_1$ (see Figure 8A) the rate for the 4-ATP formation can be simplified to a single exponential equation as a function of k_1 (see equation 3, for clarity it has been expressed in terms of reactant and product fraction).

$$\frac{[4-ATP]_t}{[4-ATP]_\infty} = 1 - e^{-k_1 t} \qquad (3)$$

The previous assumption will be only valid if the values for k_1 and k_2 calculated from the fitting to a first order equation of the exponential decrease of the 1570 cm^{-1} SERS

band (4-NTP consumption), and the exponential increase of 1593 cm^{-1} SERS band (4-ATP formation) are similar.[52] As shown in Figure 8C the fitting of the kinetics trace of the SERS intensities at 1570 cm^{-1} (4-NTP) and at 1593 cm^{-1} (4-ATP) give rise to rates constants of 5.30×10^{-3} s^{-1} and 5.45×10^{-3} s^{-1} for k_1 and k_2, respectively, demonstrating the validity of the assumption. Therefore the rate-limiting step of the reaction was the formation of the intermediate and the observed rate constant, k_{obs}, will be essentially determined by k_1.

The immobilization of the reactant on the nanoparticles surface is demonstrated through the independence of the pseudo-first order rate constants k_{obs} (k_1) with the concentration of Au@Pd NRs. As observed in Figure 8D similar k_{obs} were obtained for different amounts of catalyst. Moreover, if the rate-limiting step of the reaction is the formation of the intermediate, $k_{obs} \approx k_1$, and the reaction rate will solely depend on the borohydride concentration,

$$k_{obs} = k_1 = k_{nor}\,[NaBH_4] \qquad (4)$$

where $[NaBH_4]$ is the sodium borohydride concentration and k_{nor} the normalized rate constant considering a saturated monolayer of 4-NTP preadsorbed on the Au@Pd NRs surface. Figure 8E shows the influence of the borohydride concentration on the observed first-order rate constant, observing a linear dependence. The linear least squares fitting to these data gives a value for the normalized rate constant of 10.7 ± 0.3 $s^{-1}M^{-1}$.

Previously there were several reports on the facet-dependent catalytic activity of Au and Au@Ag nanoparticles, showing higher catalytic activity for those ones with high-index facets.[56-58] In our case the Au@Pd NRs are enclosed by five {111} facets at the tips and five {100} lateral facets with surface atoms with coordination numbers of 8 and 9, respectively. Interestingly, the comparison of normalized catalytic activity, k_{nor}, with that for Au and Au@Ag nanoparticles with high-index facets reveals that the catalytic efficiency of the highly coordinated Pd surface atoms is larger, with at least a ten-fold increase, than that for the low coordinated Au surface atoms (see Table S2 in SI). This clearly demonstrates the higher catalytic efficiency of Pd towards

hydrogenation reactions compare to Au, and envisage even higher activities for Pd surface atoms with low coordination numbers, that is, with high index facets.

Conclusions

In conclusion, we theoretically and experimentally demonstrated that Au@Pd core-shell NRs exhibit significantly enhanced plasmonic properties in terms of narrow extinction and enhanced SERS, while still maintaining pure Pd-like surface properties. The PTW Au@Pd NRs were fabricated through longitudinal overgrowth of Pd on PTW Au NRs induced by the presence of bromide ions. Thus we found that bromide ions are preferentially adsorbed to the {100} lateral facets of the PTW Au seeds suppressing Pd growth on theses facets while promoting the process on the {111} tip facets ruling out any kinetic effect. This seeded growth strategy allows the modulation of the optical properties of the obtained Au@Pd hybrid nanostructures across the entire VIS-NIR region of the spectrum through the control of parameters such as amount of Pd precursor or reaction time. Importantly, the evaluation of the refractive index susceptibility demonstrated that these Au@Pd nanostructures exhibit, to the best of our knowledge, one of the highest refractive index sensitivity reported to date (1062 nm/RIU) for any plasmonic NPs and with improved FOM compared to pure Pd NRs. Furthermore, we showed that Au@Pd NRs could be used for optical sensing of hydrogen in solution or gas phase having an excellent reversible plasmonic response. Additionally, we demonstrated that enhanced plasmonic nature of Au@Pd NRs with Pd surface properties enabled the optical monitoring of catalytic conversion of 4-NTP to 4-ATP by *in situ* SERS spectroscopy. This study advances our understanding of plasmonic properties of Au@Pd NRs and revealed that Au NP supports boost their plasmonic properties. Thus, makes them attractive and alternative to pure or Ag nanostructures for LSPR and SERS based label free sensing of gases, biomolecules, and monitoring of catalytic reactions while acting as efficient catalysts. Owing to their great promise in various potential applications, these Au@Pd hetero structures are expected open new wide range of possibilities in the field of plasmonics.

ASSOCIATED CONTENT

Supporting Information available. Additional TEM and SEM images, size distribution histograms, theoretical extinction spectra, and a summary of refractive index sensitivity and catalytic activity for different nanoparticle systems. This material is available free of charge via the Internet at http://pubs.acs.org.

AUTHOR INFORMATION

Corresponding Authors

(J. P-J): juste@uvigo.es

(I. P-S): pastoriza@uvigo.es

Notes

The authors declare no competing financial interests.

ACKNOWLEDGMENT

Funding from Spanish Ministerio de Economía y Competitividad (Grants MAT2013-45168-R and MAT2016-77809-R) is gratefully acknowledge. A.L.P. and S.B. acknowledge support by the European Research Council through an ERC Starting Grant (#335078-COLOURATOMS). L. P. acknowledges the financial support from by the Alexander von Humboldt-Stiftung. V. M.-G. acknowledges the financial support from FPU scholarship from the Spanish MINECO.

REFERENCES

(1) Mayer, K. M.; Hafner, J. H. Localized Surface Plasmon Resonance Sensors. *Chem. Rev.* **2011**, *111*, 3828-3857.

(2) Mulvaney, P. Surface Plasmon Spectroscopy of Nanosized Metal Particles. *Langmuir* **1996**, *12*, 788-800.

(3) Willets, K. A.; Duyne, R. P. V. Localized Surface Plasmon Resonance Spectroscopy and Sensing. *Annu. Rev. Phys. Chem.* **2007**, *58*, 267-297.

(4) Xiong, Y.; McLellan, J. M.; Chen, J.; Yin, Y.; Li, Z.-Y.; Xia, Y. Kinetically Controlled Synthesis of Triangular and Hexagonal Nanoplates of Palladium and Their Spr/Sers Properties. *J. Amer. Chem. Soc.* **2005**, *127*, 17118-17127.

(5) Perez-Lorenzo, M. Palladium Nanoparticles as Efficient Catalysts for Suzuki Cross-Coupling Reactions. *J. Phys. Chem. Lett.* **2012**, *3*, 167-174.

(6) Chen, Y. H.; Hung, H. H.; Huang, M. H. Seed-Mediated Synthesis of Palladium Nanorods and Branched Nanocrystals and Their Use as Recyclable Suzuki Coupling Reaction Catalysts. *J. Am. Chem. Soc.* **2009**, *131*, 9114-9121.

(7) Konda, S. K.; Chen, A. C. Palladium Based Nanomaterials for Enhanced Hydrogen Spillover and Storage. *Mater. Today* **2016**, *19*, 100-108.

(8) Adams, B. D.; Chen, A. C. The Role of Palladium in a Hydrogen Economy. *Mater. Today* **2011**, *14*, 282-289.

(9) Collins, S. S. E.; Cittadini, M.; Pecharromán, C.; Martucci, A.; Mulvaney, P. Hydrogen Spillover between Single Gold Nanorods and Metal Oxide Supports: A Surface Plasmon Spectroscopy Study. *ACS Nano* **2015**, *9*, 7846-7856.

(10) Wadell, C.; Syrenova, S.; Langhammer, C. Plasmonic Hydrogen Sensing with Nanostructured Metal Hydrides. *ACS Nano* **2014**, *8*, 11925-11940.

(11) Yang, A.; Huntington, M. D.; Cardinal, M. F.; Masango, S. S.; Van Duyne, R. P.; Odom, T. W. Hetero-Oligomer Nanoparticle Arrays for Plasmon-Enhanced Hydrogen Sensing. *ACS Nano* **2014**, *8*, 7639-7647.

(12) Smith, A. F.; Harvey, S. M.; Skrabalak, S. E.; Weiner, R. G. Engineering High Refractive Index Sensitivity through the Internal and External Composition of Bimetallic Nanocrystals. *Nanoscale* **2016**, *8*, 16841-16845.

(13) Bogart, L. K.; Pourroy, G.; Murphy, C. J.; Puntes, V.; Pellegrino, T.; Rosenblum, D.; Peer, D.; Lévy, R. Nanoparticles for Imaging, Sensing, and Therapeutic Intervention. *ACS Nano* **2014**, *8*, 3107-3122.

(14) Khan, A. U.; Zhao, S.; Liu, G. Key Parameter Controlling the Sensitivity of Plasmonic Metal Nanoparticles: Aspect Ratio. *J. Phys. Chem. C* **2016**, *120*, 19353-19364.

(15) Miller, M. M.; Lazarides, A. A. Sensitivity of Metal Nanoparticle Surface Plasmon Resonance to the Dielectric Environment. *J. Phys. Chem. B* **2005**, *109*, 21556-21565.

(16) Sugawa, K.; Tahara, H.; Yamashita, A.; Otsuki, J.; Sagara, T.; Harumoto, T.; Yanagida, S. Refractive Index Susceptibility of the Plasmonic Palladium Nanoparticle: Potential as the Third Plasmonic Sensing Material. *ACS Nano* **2015**, *9*, 1895-1904.

(17) Pakizeh, T.; Langhammer, C.; Zoric, I.; Apell, P.; Kall, M. Intrinsic Fano Interference of Localized Plasmons in Pd Nanoparticles. *Nano Lett.* **2009**, *9*, 882-886.

(18) DeSantis, C. J.; Sue, A. C.; Bower, M. M.; Skrabalak, S. E. Seed-Mediated Co-Reduction: A Versatile Route to Architecturally Controlled Bimetallic Nanostructures. *ACS Nano* **2012**, *6*, 2617-2628.

(19) Sil, D.; Gilroy, K. D.; Niaux, A.; Boulesbaa, A.; Neretina, S.; Borguet, E. Seeing Is Believing: Hot Electron Based Gold Nanoplasmonic Optical Hydrogen Sensor. *ACS Nano* **2014**, *8*, 7755-7762.

(20) Huang, J.; Zhu, Y.; Lin, M.; Wang, Q.; Zhao, L.; Yang, Y.; Yao, K. X.; Han, Y. Site-Specific Growth of Au–Pd Alloy Horns on Au Nanorods: A Platform for Highly Sensitive Monitoring of Catalytic Reactions by Surface Enhancement Raman Spectroscopy. *J. Amer. Chem. Soc.* **2013**, *135*, 8552-8561.

(21) Jiang, R. B.; Qin, F.; Ruan, Q. F.; Wang, J. F.; Jin, C. J. Ultrasensitive Plasmonic Response of Bimetallic Au/Pd Nanostructures to Hydrogen. *Adv. Funct. Mater.* **2014**, *24*, 7328-7337.

(22) Chen, H. J.; Kou, X. S.; Yang, Z.; Ni, W. H.; Wang, J. F. Shape- and Size-Dependent Refractive Index Sensitivity of Gold Nanoparticles. *Langmuir* **2008**, *24*, 5233-5237.

(23) Perez-Juste, J.; Liz-Marzan, L. M.; Carnie, S.; Chan, D. Y. C.; Mulvaney, P. Electric-Field-Directed Growth of Gold Nanorods in Aqueous Surfactant Solutions. *Adv. Funct. Mater.* **2004**, *14*, 571-579.

(24) Solis, D. M.; Taboada, J. M.; Obelleiro, F.; Liz-Marzan, L. M.; de Abajo, F. J. G. Toward Ultimate Nanoplasmonics Modeling. *Acs Nano* **2014**, *8*, 7559-7570.

(25) Solís, D. M.; Taboada, J. M.; Landesa, L.; Rodríguez, J. L.; Obelleiro, F. Squeezing Maxwell's Equations into the Nanoscale. *Prog. Electromagn. Res.* **2015**, *154*, 35-50.

(26) Harrington, R. F. *Time-Harmonic Electromagnetic Fields*; Wiley & Sons: New York, 1961.

(27) Jung, S.; Shuford, K. L.; Park, S. Optical Property of a Colloidal Solution of Platinum and Palladium Nanorods: Localized Surface Plasmon Resonance. *J. Phys. Chem. C* **2011**, *115*, 19049-19053.

(28) Link, S.; El-Sayed, M. A. Size and Temperature Dependence of the Plasmon Absorption of Colloidal Gold Nanoparticles. *J. Phys. Chem. B* **1999**, *103*, 4212-4217.

(29) Huang, X. Q.; Tang, S. H.; Mu, X. L.; Dai, Y.; Chen, G. X.; Zhou, Z. Y.; Ruan, F. X.; Yang, Z. L.; Zheng, N. F. Freestanding Palladium Nanosheets with Plasmonic and Catalytic Properties. *Nat. Nanotechnol.* **2011**, *6*, 28-32.

(30) Tang, S. H.; Chen, M.; Zheng, N. F. Multifunctional Ultrasmall Pd Nanosheets for Enhanced near-Infrared Photothermal Therapy and Chemotherapy of Cancer. *Nano. Res.* **2015**, *8*, 165-174.

(31) Yu, Y.; Zhang, Q. B.; Yao, Q. F.; Xie, J. P.; Lee, J. Y. Guiding Principles in the Galvanic Replacement Reaction of an Underpotentially Deposited Metal Layer for Site-Selective Deposition and Shape and Size Control of Satellite Nanocrystals. *Chem. Mater.* **2013**, *25*, 4746-4756.

(32) Xiang, Y. J.; Wu, X. C.; Liu, D. F.; Jiang, X. Y.; Chu, W. G.; Li, Z. Y.; Ma, Y.; Zhou, W. Y.; Xie, S. S. Formation of Rectangularly Shaped Pd/Au Bimetallic Nanorods: Evidence for Competing Growth of the Pd Shell between the {110} and {100} Side Facets of Au Nanorods. *Nano Lett.* **2006**, *6*, 2290-2294.

(33) Gomez-Grana, S.; Goris, B.; Altantzis, T.; Fernandez-Lopez, C.; Carbo-Argibay, E.; Guerrero-Martinez, A.; Almora-Barrios, N.; Lopez, N.; Pastoriza-Santos, I.; Perez-Juste, J.; Bals, S.; Van Tendeloo, G.; Liz-Marzan, L. M. Au@Ag Nanoparticles: Halides Stabilize {100} Facets. *J. Phys. Chem. Lett.* **2013**, *4*, 2209-2216.

(34) Carbo-Argibay, E.; Rodriguez-Gonzalez, B.; Pastoriza-Santos, I.; Perez-Juste, J.; Liz-Marzan, L. M. Growth of Pentatwinned Gold Nanorods into Truncated Decahedra. *Nanoscale* **2010**, *2*, 2377-2383.

(35) Carrasquillo, A.; Jeng, J. J.; Barriga, R. J.; Temesghen, W. F.; Soriaga, M. P. Electrode-Surface Coordination Chemistry: Ligand Substitution and Competitive Coordination of Halides at Well-Defined Pd(100) and Pd(111) Single Crystals. *Inorg. Chim. Acta* **1997**, *255*, 249-254.

(36) Xie, S. F.; Peng, H. C.; Lu, N.; Wang, J. G.; Kim, M. J.; Xie, Z. X.; Xia, Y. N. Confining the Nucleation and Overgrowth of Rh to the {111} Facets of Pd Nanocrystal

Seeds: The Roles of Capping Agent and Surface Diffusion. *J. Amer. Chem. Soc.* **2013**, *135*, 16658-16667.

(37) Kolasinki, K. W. *Surface Science*; 2nd ed.; Wiley: New York, 2008.

(38) Peng, H. C.; Li, Z. M.; Aldahondo, G.; Huang, H. W.; Xia, Y. N. Seed-Mediated Synthesis of Pd Nanocrystals: The Effect of Surface Capping on the Heterogeneous Nucleation and Growth. *J. Phys. Chem. C* **2016**, *120*, 11754-11761.

(39) Yoo, S. H.; Lee, J. H.; Delley, B.; Soon, A. Why Does Bromine Square Palladium Off? An Ab Initio Study of Brominated Palladium and Its Nanomorphology. *Phys. Chem. Chem. Phys.* **2014**, *16*, 18570-18577.

(40) Underwood, S.; Mulvaney, P. Effect of the Solution Refractive-Index on the Color of Gold Colloids. *Langmuir* **1994**, *10*, 3427-3430.

(41) Otte, M. A.; Sepulveda, B.; Ni, W. H.; Juste, J. P.; Liz-Marzan, L. M.; Lechuga, L. M. Identification of the Optimal Spectral Region for Plasmonic and Nanoplasmonic Sensing. *ACS Nano* **2010**, *4*, 349-357.

(42) Mehra, R. Application of Refractive Index Mixing Rules in Binary Systems of Hexadecane and Heptadecane with N-Alkanols at Different Temperatures. *P Indian as-Chem Sci* **2003**, *115*, 147-154.

(43) DeSantis, C. J.; Skrabalak, S. E. Size-Controlled Synthesis of Au/Pd Octopods with High Refractive Index Sensitivity. *Langmuir* **2012**, *28*, 9055-9062.

(44) Chiu, C. Y.; Huang, M. H. Polyhedral Au-Pdcore-Shell Nanocrystals as Highly Spectrally Responsive and Reusable Hydrogen Sensors in Aqueous Solution. *Angew. Chem. Int. Ed.* **2013**, *52*, 12709-12713.

(45) Zhu, X. Z.; Zhuo, X. L.; Li, Q.; Yang, Z.; Wang, J. F. Gold Nanobipyramid-Supported Silver Nanostructures with Narrow Plasmon Linewidths and Improved Chemical Stability. *Adv. Funct. Mater.* **2016**, *26*, 341-352.

(46) Banholzer, M. J.; Harris, N.; Millstone, J. E.; Schatz, G. C.; Mirkin, C. A. Abnormally Large Plasmonic Shifts in Silica-Protected Gold Triangular Nanoprisms. *J. Phys. Chem. C* **2010**, *114*, 7521-7526.

(47) Larsson, E. M.; Alegret, J.; Kall, M.; Sutherland, D. S. Sensing Characteristics of Nir Localized Surface Plasmon Resonances in Gold Nanorings for Application as Ultrasensitive Biosensors. *Nano Lett.* **2007**, *7*, 1256-1263.

(48) Mahmoud, M. A.; El-Sayed, M. A. Gold Nanoframes: Very High Surface Plasmon Fields and Excellent near-Infrared Sensors. *J. Amer. Chem. Soc.* **2010**, *132*, 12704-12710.

(49) Charles, D. E.; Aherne, D.; Gara, M.; Ledwith, D. M.; Gun'ko, Y. K.; Kelly, J. M.; Blau, W. J.; Brennan-Fournet, M. E. Versatile Solution Phase Triangular Silver Nanoplates for Highly Sensitive Plasmon Resonance Sensing. *ACS Nano* **2010**, *4*, 55-64.

(50) Silkin, V. M.; Chernov, I. P.; Echenique, P. M.; Koroteev, Y. M.; Chulkov, E. V. Influence of Hydrogen Absorption on Low-Energy Electronic Collective Excitations in Palladium. *Phys. Rev. B* **2007**, *76*.

(51) Herves, P.; Perez-Lorenzo, M.; Liz-Marzan, L. M.; Dzubiella, J.; Lu, Y.; Ballauff, M. Catalysis by Metallic Nanoparticles in Aqueous Solution: Model Reactions. *Chem. Soc. Rev.* **2012**, *41*, 5577-5587.

(52) Zheng, G. C.; Polavarapu, L.; Liz-Marzán, L. M.; Pastoriza-Santos, I.; Pérez-Juste, J. Gold Nanoparticle-Loaded Filter Paper: A Recyclable Dip-Catalyst for Real-Time Reaction Monitoring by Surface Enhanced Raman Scattering. *Chem. Commun.* **2015**, *51*, 4572-4575.

(53) Blaser, H. U. A Golden Boost to an Old Reaction. *Science* **2006**, *313*, 312-313.

(54) Mahmoud, M. A.; Garlyyev, B.; El-Sayed, M. A. Controlling the Catalytic Efficiency on the Surface of Hollow Gold Nanoparticles by Introducing an Inner Thin Layer of Platinum or Palladium. *J. Phys. Chem. Lett.* **2014**, *5*, 4088-4094.

(55) Li, J. M.; Liu, J. Y.; Yang, Y.; Qin, D. Bifunctional Ag@Pd-Ag Nanocubes for Highly Sensitive Monitoring of Catalytic Reactions by Surface-Enhanced Raman Spectroscopy. *J. Am. Chem. Soc.* **2015**, *137*, 7039-7042.

(56) Zhang, Q. F.; Wang, H. Facet-Dependent Catalytic Activities of Au Nanoparticles Enclosed by High-Index Facets. *ACS Catal.* **2014**, *4*, 4027-4033.

(57) Zhang, Q. F.; Han, L. L.; Jing, H.; Blom, D. A.; Lin, Y.; Xing, H. L. L.; Wang, H. Facet Control of Gold Nanorods. *Acs Nano* **2016**, *10*, 2960-2974.

(58) Jing, H.; Zhang, Q. F.; Large, N.; Yu, C. M.; Blom, D. A.; Nordlander, P.; Wang, H. Tunable Plasmonic Nanoparticles with Catalytically Active High-Index Facets. *Nano Lett.* **2014**, *14*, 3674-3682.

Table of Contents Graphic